

# Uncertainty-inspired Open Set Learning for Retinal Anomaly Identification

Meng Wang<sup>1 ‡</sup>, Tian Lin<sup>2 ‡</sup>, Lianyu Wang<sup>3 ‡</sup>, Aidi Lin<sup>2</sup>, Ke Zou<sup>4</sup>,  
Xinxing Xu<sup>1</sup>, Yi Zhou<sup>5</sup>, Yuanyuan Peng<sup>6</sup>, Qingquan Meng<sup>5</sup>, Yiming Qian<sup>1</sup>,  
Guoyao Deng<sup>4</sup>, Zhiqun Wu<sup>7</sup>, Junhong Chen<sup>8</sup>, Jianhong Lin<sup>9</sup>, Mingzhi Zhang<sup>2</sup>,  
Weifang Zhu<sup>5</sup>, Changqing Zhang<sup>10</sup>, Daoqiang Zhang<sup>3</sup>,  
Rick Siow Mong Goh<sup>1</sup>, Yong Liu<sup>1</sup>, Chi Pui Pang<sup>2,11</sup>,  
Xinjian Chen<sup>5,12 (✉)</sup>, Haoyu Chen<sup>2 (✉)</sup>, Huazhu Fu<sup>1 (✉)</sup>

<sup>1</sup> Institute of High Performance Computing (IHPC), Agency for Science, Technology and Research (A\*STAR), 1 Fusionopolis Way, #16-16 Connexis, Singapore 138632, Republic of Singapore.

<sup>2</sup> Joint Shantou International Eye Center, Shantou University and the Chinese University of Hong Kong, and Medical College, Shantou University, Guangdong 515041, China.

<sup>3</sup> College of Computer Science and Technology, Nanjing University of Aeronautics and Astronautics, Jiangsu 211100, China.

<sup>4</sup> National Key Laboratory of Fundamental Science on Synthetic Vision and the College of Computer Science, Sichuan University, Sichuan 610065, China.

<sup>5</sup> School of Electronics and Information Engineering, Soochow University, Jiangsu 215006, China.

<sup>6</sup> School of Biomedical Engineering, Anhui Medical University, Anhui 230032, China.

<sup>7</sup> Longchuan People's Hospital, Heyuan, China.

<sup>8</sup> Puning People's Hospital, Jieyang, China.

<sup>9</sup> Haifeng PengPai Memory Hospital, Shanwei, China.

<sup>10</sup> College of Intelligence and Computing, Tianjin University, Tianjin 300350, China.

<sup>11</sup> Department of Ophthalmology and Visual Sciences, The Chinese University of Hong Kong, Hong Kong, China.

<sup>12</sup> State Key Laboratory of Radiation Medicine and Protection, Soochow University, Suzhou 215006, China.

<sup>‡</sup> M. Wang, T. Lin, and L. Wang are the co-first authors.

<sup>✉</sup> X. Chen, H. Chen, and H. Fu are the co-corresponding authors.

**Abstract.** Failure to recognize samples from the classes unseen during training is a major limitation of artificial intelligence in the real-world implementation for recognition and classification of retinal anomalies. We established an uncertainty-inspired open-set (UIOS) model, which was trained with fundus images of 9 retinal conditions. Besides assessing the probability of each category, UIOS also calculated an uncertainty score to express its confidence. Our UIOS model with thresholding strategy achieved an F1 score of 99.55%, 97.01% and 91.91% for the internal testing set, external target categories (TC)-JSIEC dataset and TC-unseen testing set, respectively, compared to the F1 score of 92.20%, 80.69% and 64.74% by the standard AI model. Furthermore, UIOS correctly predicted high uncertainty scores, which would prompt the need for a manual check in the datasets of non-target categories retinal diseases, low-quality fundus images, and non-fundus images. UIOS provides a robust method for real-world screening of retinal anomalies.

# 1 Introduction

Retina is part of the central nervous system responsible for phototransduction. Retinal diseases are the leading cause of irreversible blindness and visual impairment worldwide. Treatment at the early stage of disease is important to reduce serious and permanent damages. Therefore, timely diagnosis and appropriate treatment are important for preventing threatened vision and even irreversible blindness. Diagnosis of retinal diseases requires expertise of trained ophthalmologists, while there is always heavy demand for large number of patients with retinal diseases to limited number of specialists. A solution to this service gap is image-based screening that alleviates workload of ophthalmologists. Fundus photography-based screening has been shown to be successful to prevent irreversible vision impairment and blindness caused by diabetic retinopathy [1].

In recent years, deep learning, as an established but still rapidly evolving technology, has remarkably enhanced disease screening from medical imaging [2–4], including fundus photography screening for retinal diseases. The applications of deep learning in diabetic retinopathy (DR) [5–8], glaucoma [9–11] and age-related macular degeneration (AMD) [12–14] screening have achieved comparable performance with human experts. There are also some successful applications of deep learning in classifying multiple retinal diseases [15].

However, a major drawback of the standard AI models in real-world implementation is the problem of open set recognition. AI models are trained in a close set, i.e., a limited number of categories and limited characters of samples. But the real world is an open set environment, where some samples may be out of the categories in the training set or with untypical features. Previous studies have demonstrated that the performance of deep learning models declines when applied to data out of distribution (OOD), such as low-quality images and untypical cases [16–18]. Furthermore, if the testing image is a retinal disease not included in the training set, even if it is a non-fundus image, the standard AI model will still give a diagnosis of the disease category in the training data. This would lead to misdiagnosis. Meanwhile, in practice, it is impossible to collect data that cover all fundus abnormalities with sufficient sample size to train the model. Therefore, it is highly necessary to develop an open-set learning model that can accurately classify

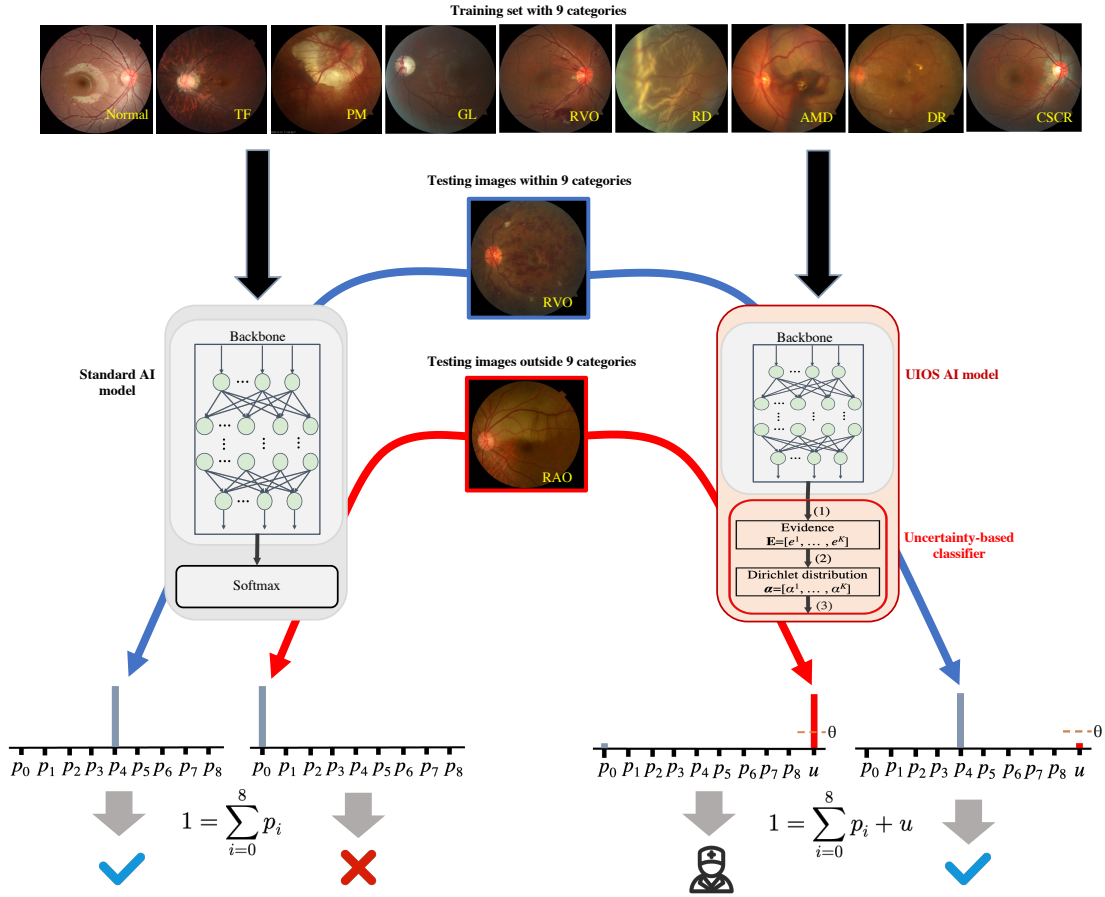


**Fig. 1:** The overview of the uncertainty-inspired open set (UIOS) learning for retinal anomaly classification. Standard artificial intelligence (AI) and UIOS AI models were trained with the same dataset with 9 categories of retinal photos. In testing, standard AI model assigns a probability value ( $p_i$ ) to each of the 9 categories, and the one with the highest probability is output as the diagnosis. Even when the model is tested with a rare retinal disease image outside of the training set, the model still outputs one from the 9 categories, which may lead to mis-diagnosis. In contrast, UIOS outputs an uncertainty score ( $\mu$ ) besides the probability ( $p_i$ ) for the 9 categories. When the model is fed with an image with obvious features of retinal disease in the 9 categories, the uncertainty-based classifier will output a prediction result with a low uncertainty score below the threshold  $\theta$  to indicate that the diagnosis result is reliable. Conversely, when the input data contains ambiguous features or is an anomaly outside of training categories, the model will assign a high uncertainty score above threshold  $\theta$  to explicitly indicate that the prediction result is unreliable and requires a double-check from their ophthalmologist to avoid mis-diagnosis.

retinal diseases included in the training set, as well as for the screening other OOD samples without the need to collect and label additional data.

In this study, we developed a novel fundamental AI model of uncertainty-inspired open set (UIOS) based on the evidential uncertainty deep neural network. As shown

**Table 1: F1 score of different models on three testing sets.**

Category	Internal testing dataset			TC-JSIEC			TC-unseen		
	Standard UIOS AI model	UIOS + model	UIOS + Thresholding	Standard UIOS AI model	UIOS + model	UIOS + Thresholding	Standard UIOS AI model	UIOS + model	UIOS + Thresholding
	Normal	97.48	99.18	99.88	72.50	84.34	90.00	75.39	83.17
TF	93.05	93.12	98.68	75.86	78.79	94.74	59.36	78.43	89.14
PM	95.98	98.84	99.39	99.08	100.00	100.00	79.90	80.00	94.69
GL	97.26	98.53	100.00	60.87	72.73	93.33	77.69	78.33	95.08
RVO	95.72	97.36	99.60	86.21	95.24	100.00	65.48	84.96	97.03
RD	93.43	99.27	100.00	97.35	94.44	98.85	48.95	72.19	92.59
AMD	87.97	97.24	99.41	83.53	93.67	99.31	42.78	50.17	76.63
DR	93.25	98.04	99.62	82.54	87.76	96.83	53.43	83.21	96.04
CSCR	75.65	94.05	99.33	68.29	77.78	100.00	79.65	83.84	93.12
Average	92.20	97.29	99.55	80.69	87.19	97.01	64.74	77.15	91.91

TF: Tigroid fundus; PM: Pathological myopia; GL: Glaucoma; RVO: Retinal vein occlusion; RD: Retinal detachment; AMD: Age-related macular degeneration; DR: Diabetic retinopathy; CSCR: Central serous chorioretinopathy.

in Fig.1, if the test data is a fundus disease included in the training set with distinct features, our proposed UIOS model will give a diagnosis decision with a low uncertainty score, which indicates that the decision is reliable. On the contrary, if the test data is in the category outside the training data set, low-quality images, and non-fundus data, UIOS will give a prediction result with a high uncertainty score, which suggests that the diagnosis result given by the AI model is unreliable. If so, a manual check by an experienced grader or ophthalmologist is required. Therefore, with the estimated uncertainty, our AI model is capable to give reliable diagnosis for retinal diseases involved in training data and avoid confusion from OOD samples.

## 2 Results

### 2.1 Performance in the internal testing dataset

In the internal testing set with 2010 images, our UIOS achieved an F1 score ranging from 93.12% to 99.27% for the 9 categories, especially for pathologic myopia (PM, 98.84%), glaucoma (GL, 98.53%), retinal detachment (RD, 99.27%), and diabetic retinopathy (DR, 98.04%) (Table 1). The average area under the curve (AUC) (Fig. 2), precision (Supplementary Table 1), F1 score (Table 1), sensitivity (Supplementary Table 2), and specificity (Supplementary Table 3) of the UIOS model were 99.79%, 97.57%, 97.29%, 97.04%,



and 99.75%, respectively, which were better than the standard AI model, although the difference was statistically significant for F1 ( $p=0.004$ ) but not AUC ( $p=0.565$ ). Furthermore, UIOS also outperformed the standard AI model in terms of confusion matrix (Supplementary Fig. 1). It should be noted that when an image is flagged as “uncertain” beyond the threshold by the UIOS model, those images are suggested to seek double checking by ophthalmologists and removed when calculating the eventual diagnostic performance metrics.

The distribution of the uncertainty score in the primary testing set was similar to the validation set, except that 9.75% of samples with uncertainty scores were above the threshold (Fig. 3 and Supplementary Table 4). After thresholding these OOD samples, the performance of UIOS was further improved. The average value of all indicators has reached more than 99%, especially the average F1 score and AUC were 99.55% and 99.89%, respectively with the UIOS+thresholding (Table 1, and Fig. 2(c)).

In addition, we compared the performance of UIOS with other commonly used uncertainty methods, including Monte-Carlo drop-out (MC-Drop), ensemble models (Ensemble), test time-augmentations (TTA), and using entropy across the categorical class probabilities in the standard AI model (Entropy). Our UIOS model consistently outperformed these uncertainty approaches in terms of F1 score, both on the original internal testing set (Supplementary Table 5) and dataset where samples with uncertainty scores above their threshold have been suggested to seek double-checking by ophthalmologists (Supplementary Table 6). Statistical analyses showed that the difference was significant except in the comparison of UIOS to Ensemble in the internal testing set with thresholding (Supplementary Table 7). The receiver operating characteristic (ROC) curves of different uncertainty methods are shown in Supplementary Fig. 2 and Supplementary Fig. 3, and the statistical analyses are shown in Supplementary Table 8. The AUCs of UIOS are higher or comparable in performance to other methods.

## 2.2 Performance in the external datasets

To further evaluate the generality of UIOS for screening fundus diseases, we also conducted experiments on two external datasets of target categories from JSIEC1000 (TC-JSIEC) and unseen target categories (TC-unseen), with 435 and 3,716 images, respec-

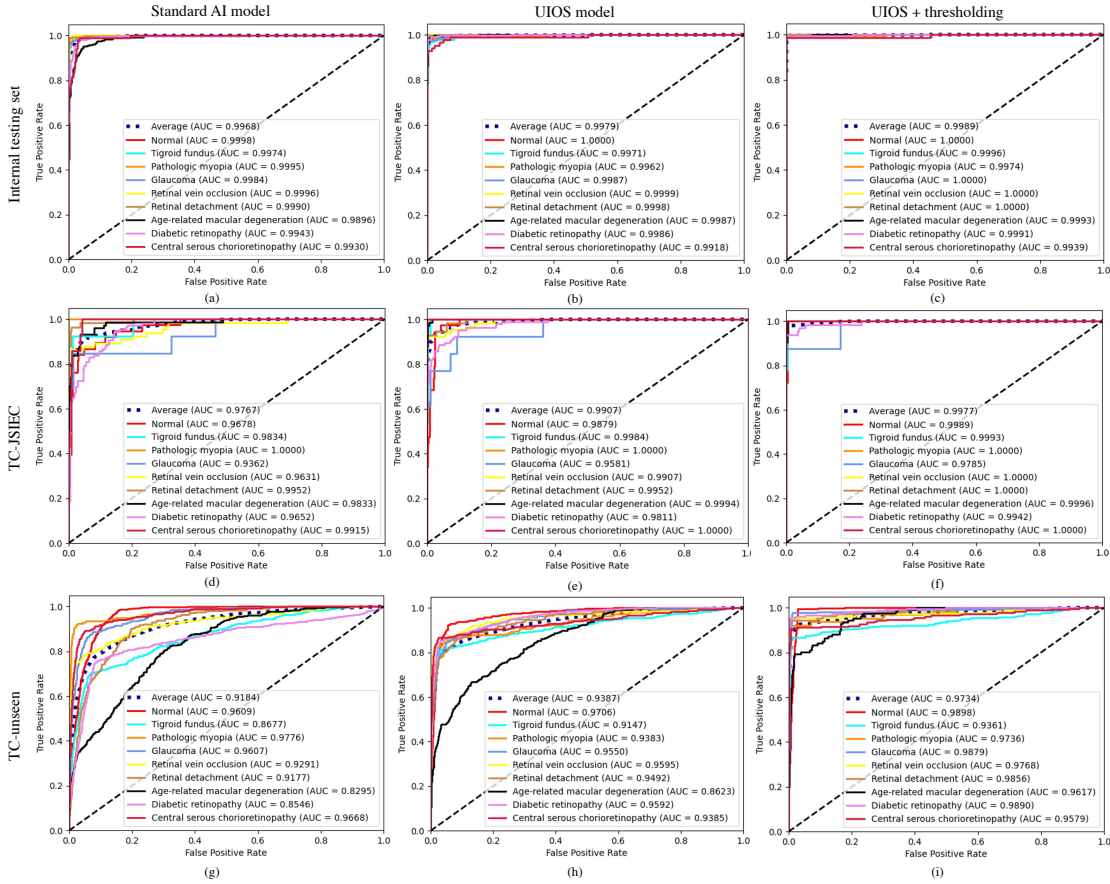


**Fig. 2: The receiver operating characteristic (ROC) curves of the standard AI model, our UIOS, and UIOS+Thresholding in internal and two external testing datasets.**

tively. Both external datasets had the same categories as the training set. The TC-JSIEC set was from a different source, while the images in the TC-unseen dataset have different features, such as early stage or ambiguous features. The performance of the standard AI model declined in these models and achieved an average F1 score of 80.69% and 64.74%, respectively (Table 1). In comparison, UIOS achieved an average F1 score of 87.19% and 77.15%, with a p value of 0.006 and 0.008, respectively, for the comparison with standard AI model (Table 1 and Supplementary Table 7). The improvement of the F1 score was found in all categories (Table 1).

There were 23.22% and 47.55% samples with an uncertainty score over the threshold, in the TC-JSIEC and TC-unseen sets, respectively (Fig. 4, Supplementary Table 4 and 9), which indicated the need for assessment by ophthalmologists. After thresholding these samples, the F1 of UIOS was further improved from 87.19% to 97.01% and from 77.15%

to 91.91%, respectively (Table 1). The precision, sensitivity, and specificity were also best in the UIOS with thresholding strategy among the three models (Supplementary Table 1-3).

The ROC curves of the three models in detecting retinal diseases in TC-JSIEC and TC-unseen datasets are shown in Fig. 2 (d-i). The AUC of the standard AI model was 97.67% and 91.84% for the TC-JSIEC and TC-unseen datasets, respectively. They improved to 99.07% and 93.87% with the UIOS model ( $p=0.002$  and  $0.185$  respectively) and further achieved 99.77% and 97.34% with the UIOS+thresholding. And, our UIOS also achieved better confusion matrices than the standard AI models on two external test sets (Supplementary Fig. 1). Furthermore, when applying our thresholding strategy (UIOS+thresholding) to indicate samples with uncertainty scores above the threshold that required manual check by ophthalmologists, we observed a further significant improvement in the confusion matrix and a significant reduction in misclassified samples (Supplementary Fig. 1).

Fig. 3 shows four samples of fundus images detected with the standard AI model and our UIOS model. The standard AI model directly took the fundus category that obtained the maximum probability value as the final diagnosis. UIOS could give the final prediction result while providing an uncertainty score to explicitly illustrate the reliability of the diagnosis. The images with lower uncertainty scores indicated higher confidence in the final decision of the model (Fig. 3 (a) and (b)). In some images with incorrect final diagnosis (Fig. 3 (c) and (d)), the standard AI model not only gave wrong prediction results, but also provided a higher probability value which led to mis-/under-diagnosis. In contrast, although UIOS could also gave wrong diagnostic results, the prediction results were indicated to be unreliable by assigning a high uncertainty score to the diagnostic results. The high uncertainty score suggested the need to seek an ophthalmologist to read the images again to prevent mis-/under-diagnosis.

We further compared the performance of our proposed UIOS to other uncertainty approaches in these two external testing sets. The results showed that our UIOS model achieved higher F1 scores (Supplementary Table 10-13) and AUC (Supplementary Fig 2 and 3) in both original datasets and the datasets after thresholding. The difference was statistically significant in most comparisons (Supplementary Table 7 and 8).

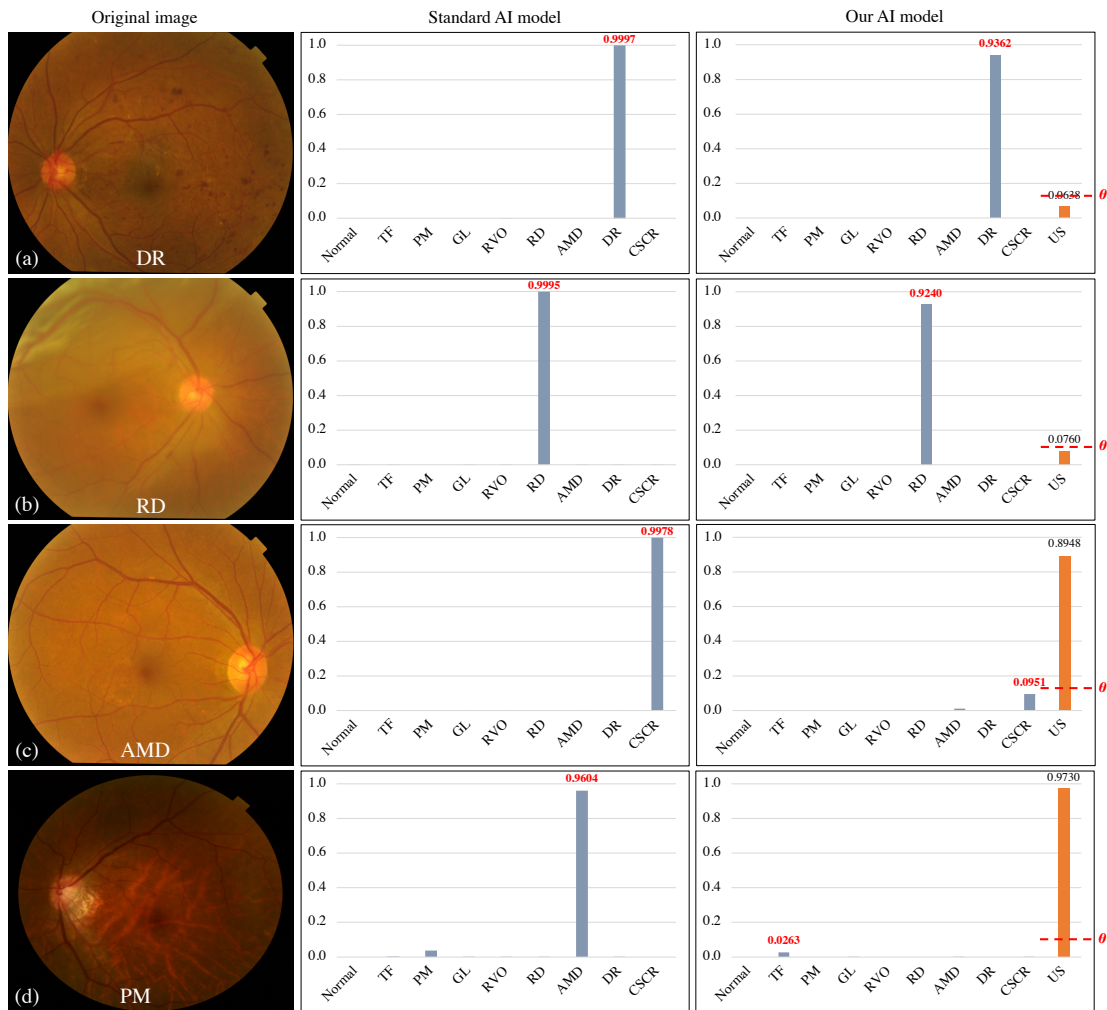


Fig. 3: Four samples of fundus images detected with the standard AI model and our UIOS model. (a)-(b) Two samples with correct diagnostic results from both the standard AI model and our UIOS model. (c)-(d) Two samples with incorrect diagnostic results from the standard AI model and our UIOS model. Unlike the standard AI model, which directly takes the fundus disease category with the highest probability score as the final diagnosis result, our UIOS will not only give the probability scores but also provide the corresponding uncertainty score to reflect the reliability of the prediction result. If the uncertainty score is less than the threshold  $\theta$ , indicating the model prediction is reliable; Conversely, if the uncertainty score is greater than the threshold  $\theta$ , which represents the result is unreliable, and manual double-checking is required to avoid possible mis-diagnosis problems. US: uncertainty score.  $\theta$ : threshold  $\theta$ .

## 2.3 Open set anomaly detection

In three fundus photo datasets with abnormal samples outside the training category, UIOS detected 86.67%, 82.27% and 89.40% of samples with high uncertainty on non-

target categories (NTC) dataset (1,380 samples), NTC-JSIEC (502 samples) and low-quality image dataset (1,066 samples), respectively. UIOS also performed well in detecting OOD samples from three non-fundus data. Specifically, UIOS achieved abnormality detection rates of 99.81%, 99.01% and 96.18% on the three non-fundus datasets RE-TOUCH [6,396 optical coherence tomography (OCT) images], OCTA [304 optical coherence tomography angiography (OCTA) images) and VOC 2012 (17,125 natural images including 21 categories), respectively. Meanwhile, Fig. 4 shows the uncertainty density distribution of different datasets outside the training set category. Compared to the uncertainty score distribution of the validation set, UIOS assigned a higher uncertainty score for the samples in different OOD datasets. In addition, Fig. 5 represents some examples of OOD images that were not included in the training category. The standard AI model provided incorrect diagnosis results and assigned a high probability to the wrongly diagnosed fundus disease. Conversely, although our UIOS model gave incorrect predictions for OOD samples, it also assigned a higher uncertainty score to indicate that the final decision was unreliable and needed assessment by an ophthalmologist.

The abnormal detection rates of different uncertainty methods on different datasets are shown in Supplementary Table 14. Overall, UIOS achieved the highest anomaly detection rates on most datasets, except in the NTC-JSIEC and OCTA datasets, where UIOS was slightly lower than Entropy and Ensemble respectively. Furthermore, our UIOS model only required a single forward pass of the model to obtain uncertainty estimates, resulting in the highest execution efficiency. Particularly when compared to MC-Drop, Ensemble, and TTA methods, UIOS showed a significant improvement in execution efficiency, with only 0.34 ms/per image (Supplementary Table 14).

### 3 Discussion

In the past few years, deep learning-based methods for the detection of retinal diseases have shown a rapid growing trend [13–15]. But less works have been reported to address the confidence and reliability of results. Besides, AI models would inevitably give wrong prediction results for rare retinal diseases or other OOD data that are not included in the training set. While we can also retrain the model to detect more abnormal classes by collecting and labeling more categories of data, it incurs more time and labor that

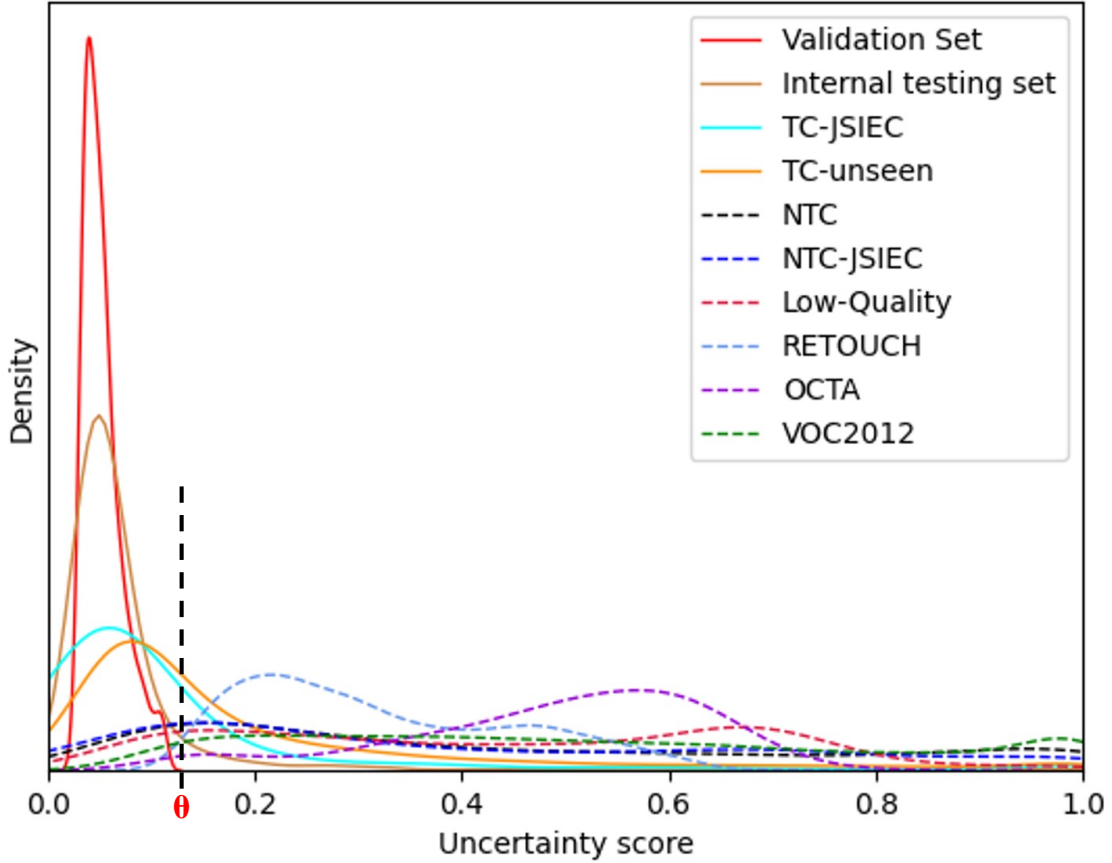


Fig. 4: Uncertainty density distribution for different datasets. Different colored solid lines indicate different test datasets for common fundus diseases, while different colored dashed lines indicate different out of distribution datasets.  $\theta$ : threshold theta.

are costly. In addition, due to limitations of medical resources and large number of patients with different fundus diseases, it is almost impossible to collect and label all the data on retinal abnormalities. This is a major reason that limits the deployment of AI models in clinical practice. To address these issues, we provide a novel uncertainty-based open-set AI model for retinal disease detection. We introduce an algorithm that divides the diagnostic results of the AI model into low and high confidence levels by uncertainty thresholding, which can significantly improve the accuracy of screening for target-categories fundus diseases in training set with obvious features, while also avoiding misdiagnosis due to ambiguous features. Our uncertainty thresholding approach can detect abnormal samples to avoid incorrect diagnosis and subsequent incidences when deploying AI models in clinical practice due to samples outside the training distribution. In addition, our proposed uncertainty paradigm is highly scalable and can be combined

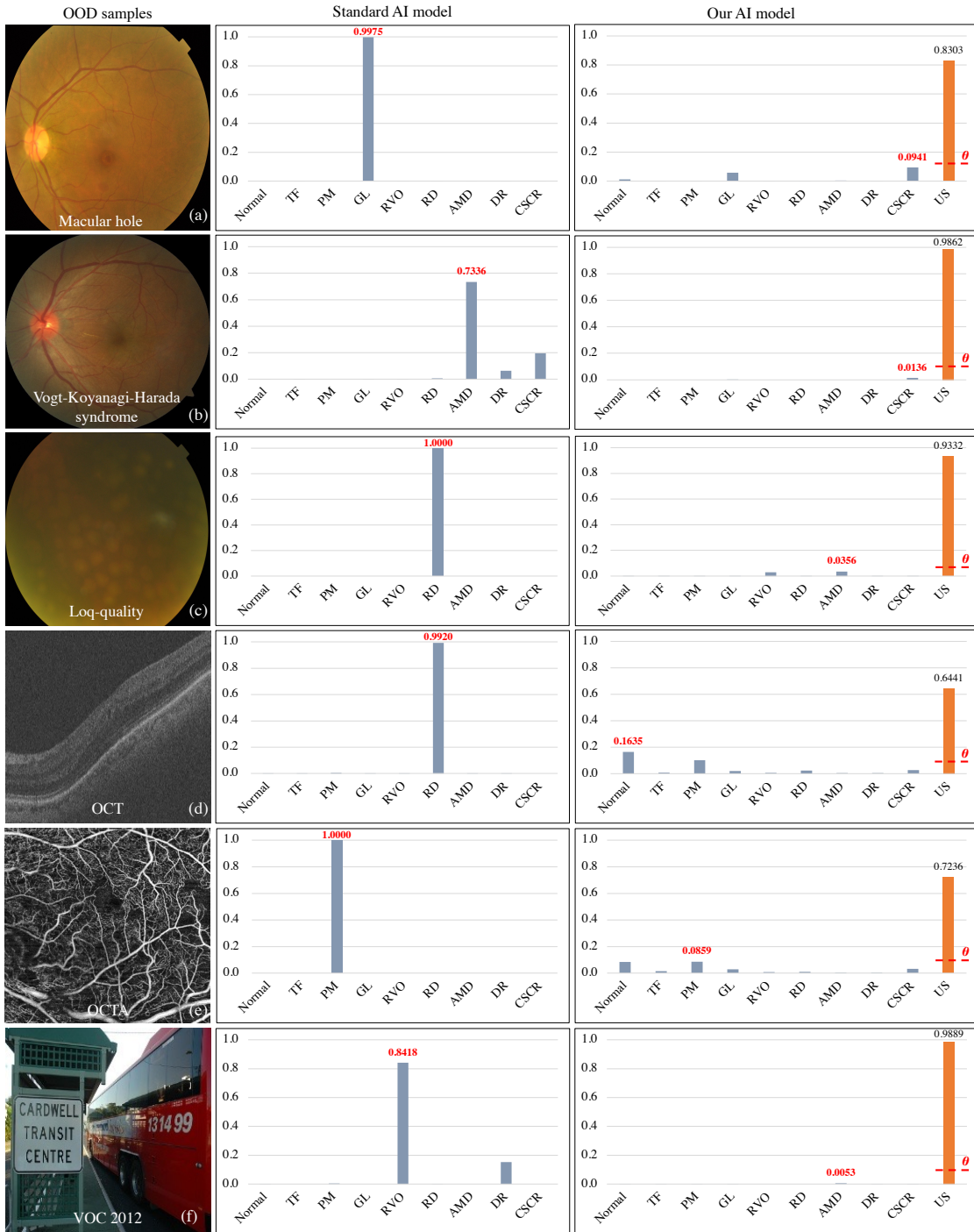


Fig. 5: Testing results of OOD samples that were not included in the training category. Besides assigning a probability to OOD samples as the standard AI model, our UIOS AI model also assigns a high uncertainty score to indicate that the final decision is unreliable and needs a double-check. US: uncertainty score.

with and enhance the performance of current commonly used baseline models for retinal diseases screening.

Recently, numerous methods have been developed to detect abnormalities in fundus images using various deep neural networks [19–22]. They trained the models with normal images only and detected abnormal images in the testing set. Although they have achieved an AUC of 0.8 to 0.9, these methods can only differentiate abnormal from normal images, but cannot classify abnormal images into different categories. Our UIOS model was developed based on multiple categories classification, including normal conditions, 8 retinal diseases, and other abnormalities. Therefore, UIOS should be adequate and ready for clinical implementation.

Several techniques have been explored to evaluate uncertainty from AI models. Bayesian neural network (BNNs) [18, 23–25] is a common uncertainty quantification approach, which can evaluate the uncertainties in their prediction. Within BNNS, MC-Drop [26] is a more scalable and commonly used method that is achieved by randomly removing a portion of nodes from the model structure when generating predictions, which also leads to higher computational costs. Deep ensemble is another uncertainty method [27, 28] which generates multiple prediction distributions by training several independent deep learning models on the same input samples and calculates the mean and variance of these distributions, where mean and variance are used as the final prediction and uncertainty. Besides, some studies explored the uncertainty evaluation based on the test time augmentation approach [29], where an input sample undergoes a series of different augmentation operations, and then the uncertainty is estimated based on the variance of prediction results from the augmented images. While there have been works exploring the application of uncertainty to medical imaging with promising performance, most of these works are based on Bayesian uncertainty and few of them are for multi-target detection of fundus images. Furthermore, there are previous works to evaluate the reliability of classification results by using entropy across the categorical class probabilities [30, 31]. While entropy is effective in capturing uncertainty within the observed classes, it may not perform well when faced with out-of-distribution examples. OOD samples can have low entropy values, leading to high confidence predictions that are incorrect. Consequently, relying solely on entropy may not provide robust detection or handling of out-of-distribution



data. Evidential-based subjective logistic uncertainty to calculate the uncertainty score is directly based on the evidence collected from the feature extractor network [32–34]. The potential capacity of subjective logistic to estimate the reliability of classification has been explored by Han et al. [33], who introduced Dirichlet distribution into subjective logical (SL) to derive probabilities of different classes and the overall uncertainty score. However, they have not explored how to detect OOD samples based on uncertainty in a quantitative approach. Our previous studies have introduced evidential uncertainty to investigate uncertainty estimation for lesion segmentation in medical images [35, 36]. Recently, two groups reported that estimating uncertainty improved the prediction of cancer by digital histopathology [37, 38]. However, the uncertainty was estimated for the binary classification. In this study, we have improved the evidential uncertainty and formalized uncertainty thresholding based on the internal validation dataset to conduct confidence evaluation on the testing datasets to detect the fundus anomaly.

In general, compared to these uncertainty approaches, there are advantages of our evidential learning-based uncertainty method: 1) Our UIOS method directly calculates the belief masses of different categories and corresponding uncertainty score by mapping the learned features from the backbone network to the space of Dirichlet parameter distribution. Therefore, our UIOS is trainable end-to-end, making it easy to implement and deploy; 2) The Dirichlet-based evidential uncertainty method provides well-calibrated uncertainty estimates. It offers reliable uncertainty measurements that align with the true confidence level of the model’s predictions, which is supported by the results of this study. This is crucial for applications where accurate assessment of uncertainty is essential, especially for medical diagnosis or critical decision-making scenarios [39, 40]. 3) Compared to other uncertainty methods like MC-Drop, ensemble, and TTA, our proposed UIOS can be computationally more efficient. It requires a single forward pass through the model to obtain uncertainty estimates, eliminating the need for multiple model runs or ensemble averaging, thus reducing the computational cost.

In ophthalmology training, junior ophthalmologists usually first learn some common retinal diseases. When they see patients in clinics, they can make diagnosis based on typical manifestations of these common retinal diseases. However, when the disease presentation is not what they have learned, the junior ophthalmologist will feel uncon-

fidet in diagnosing the patient and need to consult a senior ophthalmologist. This is a practice to avoid misdiagnosis in clinical practice. Our proposed paradigm in UIOS of uncertainty-inspired open set paradigm mimics the process of reading fundus images by junior ophthalmologists in clinical practice. The proposed uncertainty thresholding strategy enables the model to demand assessment by a human grader, i.e., a senior ophthalmologist, when the model detects high uncertainty in testing OOD samples. It can avoid potential mis-/under-diagnosis incidents in clinical practice and improve the reliability of AI models deployed in clinical practice.

We recognize limitations and the need for improvements in the current study. First, As indicated in Supplementary Table 9, 8.06%, 15.40%, and 30.09% of the samples in the internal testing set and the two external testing sets (TC-JSIEC and TC-unseen) exhibited correct predictions with higher uncertainty than the threshold, resulting in additional labor requirements. Therefore, additional efforts are necessary to enhance the UIOS’s ability to learn ambiguous features to further improve its reliability in predicting fundus diseases while reducing the need for manual reconfirmation. Second, we focused solely on classifying fundus images into one main disease category. In the next phase, we will collect more data with multi-label classifications and explore uncertainty evaluation methods for reliable multi-label diseases detection. Third, the model will be tested in more datasets. Samples with high uncertainty scores will be further assessed. Retraining will be performed with the expended dataset. Fourth, our proposed UIOS with the thresholding strategy will be applied to other image modalities (such as OCT, CT, MRI, and histopathology) and combined with artificial intelligence techniques for diagnosing specific diseases.

In conclusion, UIOS model combined with thresholding strategy is capable to accurately classify 9 retinal conditions in the training set and to detect non-target-categories retinal diseases and other OOD samples not seen during training. Our proposed UIOS model can avoid misdiagnoses and provide a robust method for screening retinal anomalies in the real world.

## 4 Methods

### 4.1 Target categories fundus photo datasets

This study was approved by the Joint Shantou International Eye Center Institutional Review Board and adhered to the principles of the Declaration of Helsinki. Data were desensitized and did not require subject notification. The data collection and labelling procedure are shown in Supplementary Fig. 4. Fundus images from 5 eye clinics with different models of fundus cameras were collected. Two trained graders performed the annotation independently. If their results were inconsistent, a retinal sub-specialist with more than 10 years experience would make the final decision. The numbers of images in each category within each dataset are listed in Supplementary Table 15.

We collected 10,034 fundus images of 8 different fundus diseases or normal condition. They were named the primary target-categories (TC) dataset. These images were randomly divided into training (6,016), validation (2,008) and test sets (2,010) in the ratio of 6:2:2. The TC included normal, tigroid fundus (TF), pathological myopia (PM), glaucoma (GL), retinal vein occlusion (RVO), retinal detachment (RD), age-related macular degeneration (AMD), diabetic retinopathy (DR), and central serous chorioretinopathy (CSCR). The inclusion criteria for these diseases are listed in Supplementary Table 16.

There may be several different features in a disease, and different patients may have different features. In human learning, junior doctors usually first learn a few features to begin with and other features later. To investigate the performance of the model in classifying images with different features from the training images, we collected 3,716 fundus images with ambiguous features of the 8 fundus diseases or normal condition as an external testing set (named as unseen target categories, TC-unseen). The including criteria are also listed in Supplementary Table 16.

To further validate the capacity of our proposed UIOS to screen retinal diseases, we also conducted experiments on the public dataset of JSIEC [15], which contained 1,000 fundus images from different subjects with 39 types of diseases and conditions. Among them, 435 fundus images were with the target categories and set as the dataset of TC-JSIEC.

## 4.2 Non-target categories fundus photo datasets

Two non-target categories retinal diseases datasets and one low quality image dataset were used to investigate the capability of UIOS to detect fundus abnormalities outside the categories of the training set. The first was 1,380 fundus images collected from the five clinics with retinal diseases outside the training set as non-target categories (NTC) dataset. The second was 502 images with fundus disease outside the training dataset in the public dataset of JSIEC and set as the dataset of non-target categories from JSIEC1000 (NTC-JSIEC). We removed the images in the categories of massive hard exudate, cotton-wool spots, preretinal hemorrhage, fibrosis and laser spots to avoid confusions caused by multiple morphologic abnormalities. The low-quality dataset was collected from the 5 clinics and consisted of 1,066 clinically unusable fundus images due to severe optical opacity, mishandling, or overexposure. The detailed diagnosis of NTC and NTC-JSIEC is listed in Supplementary Table 17.

## 4.3 Non-fundus photo datasets

Three non-fundus photo public datasets were used to evaluate the performance of AI models in detecting OOD samples. The first was the VOC2012 dataset, with 17,125 natural images of 21 categories [41]. The second was RETOUCH dataset which consisted of 6,936 2-D retinal optical coherence tomography images [42]. The third was our OCTA dataset collected from our eye clinic, consisting of 304 2D retinal OCTA images.

## 4.4 Framework of the standard AI model

As shown in Fig. 1, the standard AI model consisted of a backbone network for extracting the feature information in fundus images, while a Softmax classifier layer was adopted to produce the prediction results based on the features from the backbone network. For deep learning based disease detections, pre-trained ResNet-50 [43] has been widely used as a backbone network to extract the rich feature information contained in medical images and have achieved excellent performance [44–47]. Therefore, in this study, we employed pre-trained ResNet-50 as our backbone network to conduct experiments. As shown in Fig. 1, standard AI model assigned a probability value to each category of fundus diseases that were included in the training set. The category with the highest probability value

was output as the final diagnosis result, without any information reflecting the reliability of the final decision. However, when the standard AI model was given a fundus image of an anomaly out of the fundus diseases in the training set or non-fundus data, the model still output a category of fundus disease from the training set as the final diagnosis result, which could lead to serious mis-/under-diagnosis.

## 4.5 Framework of UIOS

As shown in Fig. 1, our proposed UIOS architecture was simple and mainly consisted of a backbone network to capture feature information. An uncertainty-based classifier was used to generate the final diagnosis result with an uncertainty score that led to more reliable decision making without losing accuracy. To ensure experimental objectivity, we adopted pre-trained ResNet-50 as our backbone to capture the feature information contained in fundus images. Meanwhile, with fundus images through ResNet-50, the final decision and corresponding overall uncertainty score were obtained by our uncertainty-based classifier, which was mainly composed of three steps. Specifically, this was a K-class retinal fundus disease detection.

**Step (1):** Obtaining the evidence feature  $E = [e_1, \dots, e_K]$  for different fundus diseases by applying Softplus activation function to ensure the feature values are larger than 0:

$$E = \text{Softplus}(F_{Out}), \quad (1)$$

where  $F_{Out}$  is the feature information obtained from the ResNet-50 backbone.

**Step (2):** Parameterizing  $E$  to Dirichlet distribution, as:

$$\boldsymbol{\alpha} = E + 1, \text{ i.e., } \alpha_k = e_k + 1, \quad (2)$$

where  $\alpha_k$  and  $e_k$  are the  $k$ -th category Dirichlet distribution parameters and evidence, respectively.

**Step (3):** Calculating the belief masses and corresponding uncertainty score as:

$$b_k = \frac{e_k}{S} = \frac{\alpha_k - 1}{S}, \quad u = \frac{K}{S}, \quad (3)$$

where  $S = \sum_{k=1}^K (e_k + 1) = \sum_{k=1}^K \alpha_k$  is the Dirichlet intensities. It can be seen from Eq. 3 the probability assigned to category  $k$  is proportional to the observed evidence for category  $k$ . Conversely, if less total evidence was obtained, the greater the total uncertainty. The belief assignment can be considered as a subjective opinion. The probability of  $k$ -th retinal fundus disease was computed as  $p_k = \frac{\alpha_k}{S}$  based on the Dirichlet distribution [48] (The definition of Dirichlet distribution is detailed in Sec. 4.6). In addition, to further improve the performance of our UIOS, we also explore a novel loss function to guide the optimization of our UIOS, the details are shown in Sec. 4.7.

## 4.6 Definition of Dirichlet distribution

The Dirichlet distribution was parameterized by its concentration  $K$  parameters  $\boldsymbol{\alpha} = [\alpha_1, \dots, \alpha_K]$ . Therefore, the probability density function of the Dirichlet distribution is computed as follows:

$$D(\mathbf{P} \mid \boldsymbol{\alpha}) = \begin{cases} \frac{1}{B(\boldsymbol{\alpha})} \prod_{k=1}^K p_k^{\alpha_k - 1} & \text{for } P \in S_K, \\ 0 & \text{otherwise,} \end{cases} \quad (4)$$

where  $S_K$  is the  $K$ -dimensional unit simplex, as follows:

$$S_K = \left\{ \mathbf{P} \mid \sum_{k=1}^K p_i = 1 \right\}, \quad 0 \leq p_i \leq 1, \quad (5)$$

where  $B(\boldsymbol{\alpha})$  represent the  $K$ -dimensional multinomial beta function.

## 4.7 Loss function

Cross entropy loss function has been widely employed in most previous diseases detection studies,

$$L_{CE} = - \sum_{k=1}^K y_k \log(p_k), \quad (6)$$

In our work, subjective logical (SL) associates the Dirichlet distribution with the belief distribution under the framework of evidential uncertainty theory to obtain the probabilities of different fundus diseases and the corresponding overall uncertainty score based on the evidence collected from the backbone network. Therefore, we could work out the

Dirichlet distribution parameter of  $\alpha = [\alpha_1, \dots, \alpha_K]$  and obtain the multinomial opinions  $D(p_i|\alpha_i)$ , where  $p_i$  is the class assignment probabilities on a simplex. Similar to TMC [33], CE loss was modified as follows:

$$L_{UN} = L_{UN-CE} + \lambda L_{KL}, \quad (7)$$

where  $L_{UN-CE}$  was used to ensure that the correct prediction for each sample yielded more evidence than other classes, while  $L_{KL}$  was employed to ensure that incorrect predictions would yield less evidence, and  $\lambda$  is the balance factor that was gradually increased so as to prevent the model from paying too much attention to the KL divergence in the initial stage of training, which might result in a lack of good exploration of the parameter space and cause the network to output a flat uniform distribution.

$$L_{UN-CE} = \int \left[ \sum_{k=1}^K -y_k \log(p_k) \right] \frac{1}{\beta(\alpha_i)} \prod_{k=1}^K p_k^{\alpha_k-1} dp_i = \sum_{k=1}^K y_i (\psi(S_k) - \psi(\alpha_k)), \quad (8)$$

where  $\psi()$  is the digamma function, while  $\beta()$  is the multinomial beta function for the concentration parameter  $\alpha$ .

$$L_{KL} = \log \left( \frac{\Gamma(\sum_{k=1}^K \hat{\alpha}_k)}{\Gamma(K) \prod_{k=1}^K \Gamma(\hat{\alpha}_k)} \right) + \sum_{k=1}^K (\hat{\alpha}_k - 1) \left[ \psi(\hat{\alpha}_k) - \psi \sum_{k=1}^K \hat{\alpha}_k \right], \quad (9)$$

where  $\hat{\alpha} = y + (1 - y) \odot \alpha$  is the adjusted parameter of the Dirichlet distribution which can avoid penalizing the evidence of the ground-truth class to 0, and  $\Gamma()$  is the gamma function.

While uncertainty loss  $L_{UN}$  can guide the model optimization based on the feature distribution which was parameterized by Dirichlet concentration. However, Dirichlet concentration also changes the original feature distribution, which may cause a decline in the classifier's confidence in the parameterized features, thus resulting in a limited performance. Therefore, to ensure confidence for the parameterized features during training, we further introduce the temperature cross-entropy loss ( $L_{TCE}$ ) to directly guide the

model optimization based on the parameterized features.

$$L_{TCE} = - \sum_{k=1}^K y_k \log \left( \frac{b_k}{\tau} \right), \quad (10)$$

where  $b_k$  was the belief mass for  $k$ -th class, while  $\tau$  was the temperature coefficients to adjust the belief values distribution, the value is initialized 0.01 was gradually increased to 1 to prevent the low confidence for the belief mass distribution in the initial stage of training.

Therefore, the final loss function for optimizing our proposed model was formalized as (The ablation experiments on the effectiveness of the loss function were shown in Supplementary Table 18):

$$L_{TUN} = L_{UN} + L_{TCE}, \quad (11)$$

## 4.8 Uncertainty thresholding strategy

In this study, the threshold  $\theta$  was determined using the distribution of uncertainty score in our validation dataset, as shown in Supplementary Table 5. The prediction results below the threshold  $\theta$  were more likely to be correct, i.e, diagnostic result with high confidence. Conversely, the decisions with the uncertainty score higher than  $\theta$  were considered more likely to be unreliable and needed assessment from ophthalmologist. To obtain the optimal threshold value, we calculated the ROC curve, all possible true positive rates (TPRs) and false positive rates (FPRs) for the wrong prediction of validation dataset based on wrong ground truth  $\hat{U} = [\hat{u}_1, \dots, \hat{u}_n]$  and uncertainty scores  $U = [u_1, \dots, u_n]$  for each sample in the validation dataset,  $n$  was the total number of samples in the validation dataset, and  $\hat{U}$  was obtained by:

$$\hat{u}_i = 1 - \mathbf{1}\{P_i, Y_i\}, \text{ where } \mathbf{1}\{P_i, Y_i\} = \begin{cases} 1 & \text{if } P_i = Y_i \\ 0 & \text{otherwise} \end{cases} \quad (12)$$

Where  $P_i$  and  $Y_i$  were the final prediction result and ground truth of  $i$ -th sample in validation dataset. Inspired by Youden's index [49], the objective function based on the



TPRs, TPRs, and thresholds of validation dataset is formalized as:

$$\ell(\theta) = 2 * TPRs(\theta) - FPRs(\theta), \quad (13)$$

Therefore, the final optimal threshold value is calculated by  $\theta = \arg \max_{\theta} \ell(\theta)$ . Finally, we obtained the optimal threshold  $\theta$  of 0.1158 and the confidence level of a model prediction result is,

$$C(P) = \begin{cases} u < \theta & \text{high-confidence} \\ u \geq \theta & \text{low-confidence} \end{cases}. \quad (14)$$

## 4.9 Experimental deployment

We trained our UIOS and other comparison methods including standard AI model, Monte-Carlo drop-out (MC-Drop), ensemble models, time-augmentations (TTA), using entropy across the categorical class probabilities (Entropy), on the public platform Pytorch and Nvidia Geforce RTX 3090 GPU (24G). Adam was adopted as the optimizer to optimize the model. Its initial learning rate and weight decay were set to 0.0001 and 0.0001, respectively. The batch size was set to 64. To improve the computational efficiency of the model, we resized the image to  $256 \times 256$ . Meanwhile, online random left-right flipping was applied for data augmentation. In addition, to reduce the time and effort in training multiple models for the ensemble, we used snapshot ensembles [50] to obtain multiple weights for ResNet-50 by using different checkpoints in a single training run. We also compared and analyzed the AUC and F1 scores of different methods.

## Code Availability

All codes are available at <https://github.com/wangmeng9218/UIOS>

## Data Availability

Data from JSIEC1000 is available at: (<https://www.kaggle.com/datasets/linchundan/fundusimage1000>).

Data from **RETOUCH** is available at: (<https://retouch.grand-challenge.org>).

Data from **VOC2012** is available at: (<http://host.robots.ox.ac.uk/pascal/VOC/voc2012>).

Additional data sets supporting the findings of this study were not publicly available due to the confidentiality policy of the Chinese National Health Council and institutional patient privacy regulations. However, they were available from the corresponding authors upon request. For replication of the findings and/or further academic and AI-related research activities, data may be requested from corresponding author H. Chen within 10 working days. Source data are provided in this paper.

## Acknowledgements

This research is supported by Agency for Science, Technology and Research (A\*STAR) Central Research Fund (“Robust and Trustworthy AI system for Multi-modality Healthcare” to H. F.), Career Development Fund (C222812010 to H. F.), A\*STAR Advanced Manufacturing and Engineering (AME) Programmatic Fund (A20H4b0141 to Y. L.), the National Key R&D Program of China (2018 YFA0701700 to H. C. and X. C.), the National Nature Science Foundation of China (U20A20170 to X. C.), Shantou Science and Technology Program (190917085269835 to H. C.), and 2020 Li Ka Shing Foundation Cross-Disciplinary Research Grant (2020LKSFG14B to H. C.).

## Author Contributions Statement

**Meng Wang:** Conceptualization, Methodology, Data collection, Experimental deployment, Software, Writing - original draft. **Tian Lin:** Data collection & annotation & curation, review & editing. **Lianyu Wang:** Data collection & curation, Experimental deployment, review & editing. **Aidi Lin:** Data collection & annotation & curation. **Ke Zou, Daoqiang Zhang, Qingquan Meng, Changqing Zhang, Yiming Qian, Guoyao Deng, Yi Zhou, Yuanyuan Peng, and Weifang Zhu:** Methodology, Writing - review & editing. **Xinxing Xu, Yong Liu, and Rick Siow Mong Goh:** Project administration, Writing - review. **Zhiqun Wu, Junhong Chen, Jianhong Lin, Mingzhi Zhang, and Chi Pui Pang:** Data collection, Clinical support, Writing - review &

editing. **Haoyu Chen:** Supervision, Data collection & annotation & curation, Clinical support, Writing - review & editing. **Xinjian Chen and Huazhu Fu:** Supervision, Project administration, Methodology, Writing - review & editing.

## Competing Interests Statement

The authors declare no competing interests.

## References

1. P. H. Scanlon, "The contribution of the english nhs diabetic eye screening programme to reductions in diabetes-related blindness, comparisons within europe, and future challenges," *Acta Diabetologica*, vol. 58, pp. 521–530, 2021.
2. V. Gulshan, L. Peng, M. Coram *et al.*, "Development and Validation of a Deep Learning Algorithm for Detection of Diabetic Retinopathy in Retinal Fundus Photographs," *JAMA*, vol. 316, no. 22, p. 2402, dec 2016.
3. D. S. W. Ting, C. Y.-L. Cheung, G. Lim *et al.*, "Development and Validation of a Deep Learning System for Diabetic Retinopathy and Related Eye Diseases Using Retinal Images From Multiethnic Populations With Diabetes," *JAMA*, vol. 318, no. 22, p. 2211, dec 2017.
4. G. Litjens, T. Kooi, B. E. Bejnordi, A. A. A. Setio, F. Ciompi, M. Ghafoorian, J. A. Van Der Laak, B. Van Ginneken, and C. I. Sánchez, "A survey on deep learning in medical image analysis," *Medical image analysis*, vol. 42, pp. 60–88, 2017.
5. V. Bellemo, Z. W. Lim, G. Lim, Q. D. Nguyen, Y. Xie, M. Y. Yip, H. Hamzah, J. Ho, X. Q. Lee, W. Hsu *et al.*, "Artificial intelligence using deep learning to screen for referable and vision-threatening diabetic retinopathy in africa: a clinical validation study," *The Lancet Digital Health*, vol. 1, no. 1, pp. e35–e44, 2019.
6. Y. Xie, Q. D. Nguyen, H. Hamzah, G. Lim, V. Bellemo, D. V. Gunasekeran, M. Y. Yip, X. Q. Lee, W. Hsu, M. L. Lee *et al.*, "Artificial intelligence for teleophthalmology-based diabetic retinopathy screening in a national programme: an economic analysis modelling study," *The Lancet Digital Health*, vol. 2, no. 5, pp. e240–e249, 2020.
7. E. Ipp, D. Liljenquist, B. Bode, V. N. Shah, S. Silverstein, C. D. Regillo, J. I. Lim, S. Sadda, A. Domalpally, G. Gray *et al.*, "Pivotal evaluation of an artificial intelligence system for autonomous detection of referable and vision-threatening diabetic retinopathy," *JAMA network open*, vol. 4, no. 11, pp. e2134254–e2134254, 2021.
8. P. Burlina, W. Paul, P. Mathew, N. Joshi, K. D. Pacheco, and N. M. Bressler, "Low-shot deep learning of diabetic retinopathy with potential applications to address artificial intelligence bias in retinal diagnostics and rare ophthalmic diseases," *JAMA ophthalmology*, vol. 138, no. 10, pp. 1070–1077, 2020.

9. E. L. Mayro, M. Wang, T. Elze, and L. R. Pasquale, "The impact of artificial intelligence in the diagnosis and management of glaucoma," *Eye*, vol. 34, no. 1, pp. 1–11, 2020.
10. M. Wang, L. Q. Shen, L. R. Pasquale, M. V. Boland, S. R. Wellik, C. G. De Moraes, J. S. Myers, T. D. Nguyen, R. Ritch, P. Ramulu *et al.*, "Artificial intelligence classification of central visual field patterns in glaucoma," *Ophthalmology*, vol. 127, no. 6, pp. 731–738, 2020.
11. M. Wang, J. Tichelaar, L. R. Pasquale, L. Q. Shen, M. V. Boland, S. R. Wellik, C. G. De Moraes, J. S. Myers, P. Ramulu, M. Kwon *et al.*, "Characterization of central visual field loss in end-stage glaucoma by unsupervised artificial intelligence," *JAMA ophthalmology*, vol. 138, no. 2, pp. 190–198, 2020.
12. T. Perepelkina and A. B. Fulton, "Artificial intelligence (ai) applications for age-related macular degeneration (amd) and other retinal dystrophies," in *Seminars in ophthalmology*, vol. 36, no. 4. Taylor & Francis, 2021, pp. 304–309.
13. A. Bhuiyan, T. Y. Wong, D. S. W. Ting, A. Govindaiah, E. H. Souied, and R. T. Smith, "Artificial intelligence to stratify severity of age-related macular degeneration (amd) and predict risk of progression to late amd," *Translational vision science & technology*, vol. 9, no. 2, pp. 25–25, 2020.
14. Y. Peng, Q. Chen, T. D. Keenan, E. Y. Chew, and Z. Lu, "Artificial intelligence in age-related macular degeneration (amd)," *Artificial Intelligence in Ophthalmology*, pp. 101–112, 2021.
15. L.-P. Cen, J. Ji, J.-W. Lin, S.-T. Ju, H.-J. Lin, T.-P. Li, Y. Wang, J.-F. Yang, Y.-F. Liu, S. Tan *et al.*, "Automatic detection of 39 fundus diseases and conditions in retinal photographs using deep neural networks," *Nature communications*, vol. 12, no. 1, p. 4828, 2021.
16. Y. Chen, M. Mancini, X. Zhu, and Z. Akata, "Semi-supervised and unsupervised deep visual learning: A survey," *IEEE Transactions on Pattern Analysis and Machine Intelligence*, 2022.
17. B. Li, Z. Han, H. Li, H. Fu, and C. Zhang, "Trustworthy long-tailed classification," in *Proceedings of the IEEE/CVF Conference on Computer Vision and Pattern Recognition*, 2022, pp. 6970–6979.
18. U. Upadhyay, S. Karthik, Y. Chen, M. Mancini, and Z. Akata, "Bayescap: Bayesian identity cap for calibrated uncertainty in frozen neural networks," in *Computer Vision—ECCV 2022: 17th European Conference, Tel Aviv, Israel, October 23–27, 2022, Proceedings, Part XII*. Springer, 2022, pp. 299–317.
19. K. Zhou, Y. Xiao, J. Yang, J. Cheng, W. Liu, W. Luo, Z. Gu, J. Liu, and S. Gao, "Encoding structure-texture relation with p-net for anomaly detection in retinal images," in *Computer Vision—ECCV 2020: 16th European Conference, Glasgow, UK, August 23–28, 2020, Proceedings, Part XX 16*. Springer, 2020, pp. 360–377.
20. K. Zhou, J. Li, Y. Xiao, J. Yang, J. Cheng, W. Liu, W. Luo, J. Liu, and S. Gao, "Memorizing structure-texture correspondence for image anomaly detection," *IEEE Transactions on Neural Networks and Learning Systems*, vol. 33, no. 6, pp. 2335–2349, 2021.
21. Y. Han, W. Li, M. Liu, Z. Wu, F. Zhang, X. Liu, L. Tao, X. Li, and X. Guo, "Application of an anomaly detection model to screen for ocular diseases using color retinal fundus images: design and evaluation study," *Journal of medical Internet research*, vol. 23, no. 7, p. e27822, 2021.

22. P. Burlina, W. Paul, T. A. Liu, and N. M. Bressler, "Detecting anomalies in retinal diseases using generative, discriminative, and self-supervised deep learning," *JAMA ophthalmology*, vol. 140, no. 2, pp. 185–189, 2022.
23. J. Denker and Y. LeCun, "Transforming neural-net output levels to probability distributions," *Advances in neural information processing systems*, vol. 3, 1990.
24. D. J. C. Mackay, *Bayesian methods for adaptive models*. California Institute of Technology, 1992.
25. D. J. MacKay, "A practical bayesian framework for backpropagation networks," *Neural computation*, vol. 4, no. 3, pp. 448–472, 1992.
26. Y. Gal and Z. Ghahramani, "Dropout as a bayesian approximation: Representing model uncertainty in deep learning," in *international conference on machine learning*. PMLR, 2016, pp. 1050–1059.
27. B. Lakshminarayanan, A. Pritzel, and C. Blundell, "Simple and scalable predictive uncertainty estimation using deep ensembles," *Advances in neural information processing systems*, vol. 30, 2017.
28. F. Wenzel, J. Snoek, D. Tran, and R. Jenatton, "Hyperparameter ensembles for robustness and uncertainty quantification," *Advances in Neural Information Processing Systems*, vol. 33, pp. 6514–6527, 2020.
29. G. Wang, W. Li, M. Aertsen, J. Deprest, S. Ourselin, and T. Vercauteren, "Aleatoric uncertainty estimation with test-time augmentation for medical image segmentation with convolutional neural networks," *Neurocomputing*, vol. 338, pp. 34–45, 2019.
30. G. Pereyra, G. Tucker, J. Chorowski, L. Kaiser, and G. Hinton, "Regularizing neural networks by penalizing confident output distributions," *arXiv preprint arXiv:1701.06548*, 2017.
31. T. Nair, D. Precup, D. L. Arnold, and T. Arbel, "Exploring uncertainty measures in deep networks for multiple sclerosis lesion detection and segmentation," *Medical image analysis*, vol. 59, p. 101557, 2020.
32. A. Jsang, "Subjective logic: A formalism for reasoning under uncertainty," *Springer Verlag*, 2016.
33. Z. Han, C. Zhang, H. Fu, and J. T. Zhou, "Trusted multi-view classification," *ICLR*, 2021.
34. K. Zou, Z. Chen, X. Yuan, X. Shen, M. Wang, and H. Fu, "A review of uncertainty estimation and its application in medical imaging," *Meta-Radiology*, vol. 1, no. 1, p. 100003, 2023.
35. K. Zou, X. Yuan, X. Shen, M. Wang, and H. Fu, "Tbrats: Trusted brain tumor segmentation," in *Medical Image Computing and Computer Assisted Intervention–MICCAI 2022: 25th International Conference, Singapore, September 18–22, 2022, Proceedings, Part VIII*. Springer, 2022, pp. 503–513.
36. M. Wang, K. Yu, C.-M. Feng, K. Zou, Y. Xu, Q. Meng, R. S. M. Goh, Y. Liu, X. Xu, and H. Fu, "Reliable joint segmentation of retinal edema lesions in oct images," *arXiv preprint arXiv:2212.00330*, 2022.
37. J. M. Dolezal, A. Srisuwananukorn, D. Karpeyev, S. Ramesh, S. Kochanny, B. Cody, A. S. Mansfield, S. Rakshit, R. Bansal, M. C. Bois *et al.*, "Uncertainty-informed deep learning models enable high-confidence predictions for digital histopathology," *Nature communications*, vol. 13, no. 1, p. 6572, 2022.
38. H. Olsson, K. Kartasalo, N. Mulliqi, M. Capuccini, P. Ruusuvoori, H. Samaratunga, B. Delahunt, C. Lindskog, E. A. Janssen, A. Blilie *et al.*, "Estimating diagnostic uncertainty in artificial intelligence assisted pathology using conformal prediction," *Nature communications*, vol. 13, no. 1, p. 7761, 2022.

39. J. Gawlikowski, C. R. N. Tassi, M. Ali, J. Lee, M. Humt, J. Feng, A. Kruspe, R. Triebel, P. Jung, R. Roscher *et al.*, “A survey of uncertainty in deep neural networks,” *arXiv preprint arXiv:2107.03342*, 2021.
40. M. Abdar, F. Pourpanah, S. Hussain, D. Rezazadegan, L. Liu, M. Ghavamzadeh, P. Fieguth, X. Cao, A. Khosravi, U. R. Acharya *et al.*, “A review of uncertainty quantification in deep learning: Techniques, applications and challenges,” *Information fusion*, vol. 76, pp. 243–297, 2021.
41. M. Everingham, S. A. Eslami, L. Van Gool, C. K. Williams, J. Winn, and A. Zisserman, “The pascal visual object classes challenge: A retrospective,” *International journal of computer vision*, vol. 111, pp. 98–136, 2015.
42. H. Bogunović, F. Venhuizen, S. Klmscha, S. Apostolopoulos, A. Bab-Hadiashar, U. Bagci, M. F. Beg, L. Bekalo, Q. Chen, C. Ciller *et al.*, “Retouch: the retinal oct fluid detection and segmentation benchmark and challenge,” *IEEE transactions on medical imaging*, vol. 38, no. 8, pp. 1858–1874, 2019.
43. K. He, X. Zhang, S. Ren, and J. Sun, “Deep residual learning for image recognition,” in *Proceedings of the IEEE conference on computer vision and pattern recognition*, 2016, pp. 770–778.
44. V. Kumar, H. Arora, J. Sisodia *et al.*, “Resnet-based approach for detection and classification of plant leaf diseases,” in *2020 international conference on electronics and sustainable communication systems (ICESC)*. IEEE, 2020, pp. 495–502.
45. A. Keles, M. B. Keles, and A. Keles, “Cov19-cnnnet and cov19-resnet: diagnostic inference engines for early detection of covid-19,” *Cognitive Computation*, pp. 1–11, 2021.
46. M. Talo, O. Yildirim, U. B. Baloglu, G. Aydin, and U. R. Acharya, “Convolutional neural networks for multi-class brain disease detection using mri images,” *Computerized Medical Imaging and Graphics*, vol. 78, p. 101673, 2019.
47. Y. Peng, W. Zhu, Z. Chen, M. Wang, L. Geng, K. Yu, Y. Zhou, T. Wang, D. Xiang, F. Chen *et al.*, “Automatic staging for retinopathy of prematurity with deep feature fusion and ordinal classification strategy,” *IEEE Transactions on Medical Imaging*, vol. 40, no. 7, pp. 1750–1762, 2021.
48. K. W. Ng, G.-L. Tian, and M.-L. Tang, “Dirichlet and related distributions: Theory, methods and applications,” 2011.
49. N. J. Perkins and E. F. Schisterman, “The youden index and the optimal cut-point corrected for measurement error,” *Biometrical Journal: Journal of Mathematical Methods in Biosciences*, vol. 47, no. 4, pp. 428–441, 2005.
50. G. Huang, Y. Li, G. Pleiss, Z. Liu, J. E. Hopcroft, and K. Q. Weinberger, “Snapshot ensembles: Train 1, get m for free,” *arXiv preprint arXiv:1704.00109*, 2017.

# Supplementary files

Supplementary Table 1: Precision of different models on different testing sets (%)

Category	Internal testing set			TC-JSIEC			TC-unseen		
	Standard AI model	UIOS	UIOS + Thresholding	Standard AI model	UIOS	UIOS + Thresholding	Standard AI model	UIOS	UIOS + Thresholding
Normal	95.08	98.38	99.76	69.05	77.78	81.82	62.49	76.77	87.10
TF	95.60	94.62	98.68	68.75	65.00	90.00	74.33	81.72	95.90
PM	95.43	99.42	100.00	98.18	100.00	100.00	82.50	81.16	98.31
GL	100.00	99.50	100.00	70.00	88.89	100.00	76.49	75.05	92.96
RVO	96.85	95.56	99.21	100.00	100.00	100.00	92.46	90.37	99.49
RD	88.24	98.91	100.00	98.21	100.00	100.00	35.89	69.32	91.74
AMD	96.30	96.91	99.21	73.96	88.10	98.63	53.67	57.71	74.07
DR	95.30	98.48	99.62	93.98	95.56	100.00	65.06	85.21	96.89
CSCR	68.22	96.34	100.00	51.85	63.64	100.00	76.05	82.08	95.56
Average	92.34	97.57	99.61	80.44	86.55	96.72	68.77	77.71	92.45

Supplementary Table 2: Sensitivity of different models on different testing sets (%)

Category	Internal testing set			TC-JSIEC			TC-unseen		
	Standard AI model	UIOS	UIOS + Thresholding	Standard AI model	UIOS	UIOS + Thresholding	Standard AI model	UIOS	UIOS + Thresholding
Normal	100.00	100.00	100.00	76.32	92.11	100.00	95.01	90.73	99.43
TF	90.63	91.67	98.68	84.62	100.00	100.00	49.40	75.40	83.27
PM	96.53	98.27	98.80	100.00	100.00	100.00	77.46	78.87	91.34
GL	94.66	97.57	100.00	53.85	61.54	87.50	78.93	81.91	97.29
RVO	94.62	99.23	100.00	75.76	90.91	100.00	50.69	80.17	94.69
RD	99.26	99.63	100.00	96.49	89.47	97.73	76.95	75.31	93.46
AMD	80.97	97.58	99.60	95.95	100.00	100.00	35.56	44.38	79.37
DR	91.29	97.60	99.62	73.58	81.13	93.85	45.33	81.31	95.20
CSCR	84.88	91.86	98.67	100.00	100.00	100.00	83.60	85.68	90.80
Average	92.54	97.04	99.49	84.06	90.57	97.67	65.88	77.08	91.65



Supplementary Table 3: Specificity of different models on different testing sets (%)

Category	Internal testing set			TC-JSIEC			TC-unseen		
	Standard AI model	UIOS	UIOS + Thresholding	Standard AI model	UIOS	UIOS + Thresholding	Standard AI model	UIOS S	UIOS + Thresholding
Normal	98.61	99.56	99.93	96.73	97.48	98.73	89.86	95.12	96.74
TF	99.79	99.74	99.94	98.82	98.34	99.69	97.32	97.35	99.40
PM	99.56	99.95	100.00	99.74	100.00	100.00	99.00	98.89	99.89
GL	100.00	99.94	100.00	99.29	99.76	100.00	96.20	95.74	98.88
RVO	99.79	99.68	99.94	100.00	100.00	100.00	99.55	99.08	99.94
RD	97.93	99.83	100.00	99.74	100.00	100.00	90.38	97.67	99.51
AMD	99.48	99.48	99.87	93.07	97.23	99.62	97.02	96.84	98.08
DR	99.11	99.70	99.94	98.48	98.78	100.00	95.62	97.46	99.59
CSCR	98.23	99.84	100.00	96.91	98.10	100.00	96.53	97.53	99.35
Average	99.17	99.75	99.96	98.09	98.86	99.78	95.72	97.30	99.04

Supplementary Table 4: Distribution of data after filtering out samples with uncertainty scores above the threshold value of  $\theta$ 

Dataset	Internal testing set		TC-JSIEC		TC-unseen	
	Original	After thresholding	Original	After thresholding	Original	After thresholding
Normal	425	423	38	18	561	353
TF	96	76	13	9	504	281
PM	173	166	54	53	213	127
GL	206	183	13	8	503	258
RVO	130	126	66	51	363	207
RD	272	252	57	44	243	107
AMD	289	252	74	72	329	126
DR	333	261	106	65	567	229
CSCR	86	75	14	14	433	261
Total	2,010	1,814	435	334	3,716	1,949

Supplementary Table 4 shows the distribution of different testing sets after filtering out samples with uncertainty scores above the threshold value of  $\theta$ . As shown in Supplementary Table 4, most of the samples in the internal testing set, which have a similar feature distribution to the training data, obtained high-confidence prediction results. However, the two external test data sets, TC-JSIEC and TC-unseen, have a large difference in feature distribution from the training data. Consequently, more samples from these sets required double-checking by the ophthalmologist to avoid mis-/under-diagnosis may be caused by the samples with low confidence prediction results. These results are consistent with the observation in clinical practice that junior physicians can accurately identify fundus diseases with distinctive features with high confidence. However, data with ambiguous features are often judged with low confidence, and it is necessary to seek further confirmation from a senior ophthalmologist before a final diagnosis can be made.

Supplementary Table 5: F1 scores of different methods on internal testing set (%)

Category	MC-Drop	Ensemble	TTA	Entropy	UIOS
Normal	99.05	97.69	97.79	97.67	99.18
TF	95.43	94.18	90.00	91.30	93.12
PM	91.54	97.66	95.51	95.18	98.84
GL	91.31	93.58	92.52	93.09	98.53
RVO	93.63	96.44	96.53	96.12	97.36
RD	95.64	96.38	92.51	92.13	99.27
AMD	90.65	90.98	85.77	85.60	97.24
DR	95.20	95.41	91.56	91.04	98.04
CSCR	87.06	89.02	82.29	81.03	94.05
Average	93.28	94.59	91.61	91.46	97.29

Supplementary Table 6: F1 scores of different methods on internal testing set after thresholding (%)

Category	MC-Drop	Ensemble	TTA	Entropy	UIOS
Normal	99.87	99.37	99.60	99.88	99.88
TF	97.56	98.59	96.92	98.99	98.68
PM	97.44	99.66	97.58	100.00	99.39
GL	97.71	99.49	97.17	99.73	100.00
RVO	99.07	98.36	98.06	99.53	99.60
RD	99.40	99.18	97.05	99.38	100.00
AMD	97.23	98.98	92.45	98.54	99.41
DR	98.84	98.87	96.72	99.44	99.62
CSCR	98.97	95.45	90.43	96.00	99.33
Average	98.45	98.66	96.22	99.05	99.55

Supplementary Table 7: P-values of F1 scores for UIOS model compared to other methods on different datasets

Methods	Internal testing set	TC-JSIEC	TC-unseen	Internal testing set+thresholding	TC-JSIEC+thresholding	TC-unseen dataset+thresholding
UIOS->Baseline	<b>0.029</b>	<b>0.006</b>	<b>0.008</b>	/	/	/
UIOS->MC-Drop	<b>0.008</b>	<b>0.026</b>	<b>0.001</b>	<b>0.005</b>	0.091	<b>0.004</b>
UIOS->Ensemble	<b>0.009</b>	0.376	<b>0.001</b>	0.058	0.286	<b>0.009</b>
UIOS->Entropy	<b>0.004</b>	<b>0.045</b>	<b>0.001</b>	0.235	<b>0.046</b>	<b>0.027</b>
UIOS->TTA	<b>0.003</b>	<b>0.030</b>	<b>0.001</b>	<b>0.007</b>	<b>0.042</b>	<b>0.0002</b>

P-Value was calculated by two-sided T-Test, and no adjustments were made for multiple comparisons.

Supplementary Table 8: P-values of AUC for UIOS model compared to other methods on different datasets

Methods	Internal testing set	TC-JSIEC	TC-unseen	Internal testing set+thresholding	TC-JSIEC+thresholding	TC-unseen dataset+thresholding
UIOS->Baseline	0.371	<b>0.002</b>	0.196	/	/	/
UIOS->MC-Drop	<b>0.036</b>	0.055	<b>0.003</b>	0.058	0.115	<b>0.006</b>
UIOS->Ensemble	<b>0.036</b>	0.219	<b>0.036</b>	0.071	0.276	<b>0.033</b>
UIOS->Entropy	0.565	<b>0.020</b>	0.610	0.263	<b>0.029</b>	0.259
UIOS->TTA	<b>0.032</b>	<b>0.023</b>	<b>0.010</b>	<b>0.017</b>	<b>0.015</b>	<b>0.005</b>

P-Value was calculated by two-sided T-Test, and no adjustments were made for multiple comparisons.

Supplementary Table 9: Rates for prompting a human grading and correct disease prediction with high uncertainty above threshold

Category	Internal testing set (%)	TC-JSIEC(%)	TC-unseen dataset (%)
Rate for prompting a human grading	9.75	23.22	47.55
Rate of correct disease prediction with high uncertainty above threshold	8.06	15.40	30.09

Supplementary Table 10: F1 scores of different methods on TC-JSIEC set (%)

Category	MC-Drop	Ensemble	TTA	Entropy	UIOS
Normal	34.78	67.53	57.14	58.06	84.34
TF	72.73	81.25	81.48	85.71	78.79
PM	97.20	99.08	94.64	94.64	100.00
GL	60.87	80.00	56.00	56.00	72.73
RVO	84.75	89.08	90.32	90.32	95.24
RD	92.45	96.36	91.43	91.43	94.44
AMD	74.00	93.08	87.50	87.50	93.67
DR	86.01	88.44	86.73	86.73	87.76
CSCR	59.09	70.00	48.28	48.28	77.78
Average	73.54	84.98	77.06	77.63	87.19



Supplementary Table 11: F1 scores of different methods on TC-unseen dataset (%)

Category	MC-Drop	Ensemble	TTA	Entropy	UIOS
Normal	65.97	72.54	74.91	74.21	83.17
TF	55.43	49.94	55.67	54.17	78.43
PM	45.36	72.22	66.24	65.38	80.00
GL	69.00	73.00	74.20	74.37	78.33
RVO	67.01	60.23	65.34	65.21	84.96
RD	61.28	60.68	60.64	61.84	72.19
AMD	47.72	44.05	39.06	39.14	50.17
DR	72.00	69.68	79.28	79.47	83.21
CSCR	73.99	74.53	75.35	74.84	83.84
Average	61.97	64.10	65.63	65.40	77.15

Supplementary Table 12: F1 scores of different methods on TC-JSIEC set after thresholding (%)

Category	MC-Drop	Ensemble	TTA	Entropy	UIOS
Normal	22.22	66.67	63.64	40.00	90.00
TF	92.31	100.00	100.00	50.00	94.74
PM	100.00	100.00	96.91	99.05	100.00
GL	90.91	100.00	76.92	66.67	93.33
RVO	91.30	91.18	95.15	95.83	100.00
RD	100.00	100.00	93.33	98.36	98.85
AMD	85.31	96.97	95.33	95.74	99.31
DR	89.71	98.63	91.34	98.46	96.83
CSCR	76.19	85.71	61.54	88.00	100.00
Average	83.11	93.24	86.02	81.35	97.01

Supplementary Table 13: F1 scores of different methods on TC-unseen dataset after thresholding (%)

Category	MC-Drop	Ensemble	TTA	Entropy	UIOS
Normal	82.89	78.15	84.64	87.68	92.86
TF	72.89	55.59	58.48	55.46	89.14
PM	45.28	84.54	77.08	88.24	94.69
GL	84.40	92.60	83.29	94.31	95.08
RVO	74.56	63.89	68.92	80.19	97.03
RD	81.40	84.48	65.95	85.11	92.59
AMD	58.71	73.91	48.00	70.00	76.63
DR	81.91	80.31	84.33	93.46	96.04
CSCR	87.92	89.81	80.88	89.49	93.12
Average	74.44	78.14	72.40	82.66	91.91

Supplementary Table 14: The abnormal detection rates of different methods on different datasets (%)

Methods	NTC	NTC-JSIEC	Low-quality	RETOUCH	OCTA	VOC 2012	Time (ms/per image)
MC-Drop	71.96	69.92	54.32	1.40	59.21	73.56	18.11
Ensemble	79.20	81.08	71.11	5.49	<b>100.00</b>	83.85	1.01
Entropy	82.61	<b>83.27</b>	84.62	2.72	0.00	44.85	<b>0.34</b>
TTA	56.30	58.37	55.63	26.10	2.96	48.90	4.87
UIOS	<b>86.67</b>	82.27	<b>89.40</b>	<b>99.81</b>	99.01	<b>96.18</b>	<b>0.34</b>

Supplementary Table 15: Sample size of the target categories datasets (%)

Dataset	Primary TC dataset				TC-unseen	TC-JSIEC
	Total	Training set	Validation set	Testing set		
Normal	2,125	1,275	425	425	561	38
TF	478	286	96	96	504	13
PM	863	517	173	173	213	54
GL	1,026	615	205	206	503	13
RVO	650	390	130	130	363	66
RD	1,359	815	272	272	243	57
AMD	1,443	865	289	289	329	74
DR	1,661	996	332	333	567	106
CSCR	429	257	86	86	433	14
Total	10,034	6,016	2,008	2,010	3,716	435

Supplementary Table 16. Inclusion criteria for Target Categories (TC) retinal diseases

Categories	Primary TC dataset	TC-unseen dataset
Normal	Orange-red fundus without any pathological changes.	Orange-red fundus without pathological changes, but maybe with indistinct C/D ratio, blurring boundary of optic disc, few exposed choroidal large vessels, overexposure or underexposure, suspicious lens stains, or generally slightly blur due to medium opacity or defocus.
Tigroid Fundus (TF)	Extensive/diffuse attenuation of RPE exposed the underlying large choroidal vessels, with an area larger than half field.	Local attenuation of the RPE with visibility of underlying regional choroidal vessels with an area less than half field.
Pathological Myopia (PM)	Extensive tigroid fundus with massive chorioretinal atrophy, Fuchs spot, lacquer cracks, CNV, subretinal hemorrhage.	Obvious tigroid fundus with tilted optic disc, optic disc arc atrophy, choroid thinning, but without massive focal chorioretinal atrophy or macular lesions. Or combined with epiretinal membrane and retinal holes leading to retinal detachment,
Glaucoma (GL)	Vertical C/D ratio $\geq 0.6$ , cup excavation and pale, thinning of neuroretinal rim, notching and bayoneting of vessels, baring of circumlinear blood vessels, laminar dot sign, disc hemorrhages, RNFL defects, peripapillary atrophy.	Enlarged C/D ratio without other classic glaucomatous damages of optic head, may with tilt, neovascularization or overexposure of optic disc. May combined with other lesions like tigroid fundus, drusen, hemorrhage, etc.
Retinal Vein Occlusion (RVO)	Tortuosity and dilatation of affected branches of veins, with variable degrees of intraretinal hemorrhage (dot-, blot- or flame-like), cotton wool spots, hard exudates, macular edema or subretinal fluid in the distribution of affected veins.	Sheathing, sclerosis or slightly dilation of affected veins, diffused/local distribution of variable hemorrhage but not strictly accompanying veins, maybe with chronic macular oedema, collateral vessels, glaucomatous optic nerve changes, retinal neovascularization, vitreous/preretinal hemorrhage or tractional retinal detachment. Laser spots may be seen.
Retinal Detachment (RD)	Detaching retina layer with a convex configuration and corrugated appearance, maybe with variable retinal breaks in view	Only small part of ambiguous detaching retina in view, or combined with other pathological lesions like massive vitreous hemorrhage, proliferative vitreoretinopathy or chorioretinal atrophy.
Age-Related Macular Degeneration (AMD)	Multiple dense or confluent drusen, focal hyper- and/or hypopigmentation of the RPE, thinning or geographic atrophy of RPE, choroidal neovascularization leading to fibrovascular/serous PED, sub-foveal atrophy or fibrosis secondary to an RPE tear	Only small or intermediate-sized drusen without other lesions, or orange-reddish bulb-like lesions associated with significant hemorrhagic and exudative detachments of retina and retinal pigment epithelium and hard exudates in polypoidal choroidal vasculopathy.
Diabetic Retinopathy (DR)	Multiple microaneurysms, variable dot/blot-like hemorrhages, hard exudates, maybe with macular oedema, neovascularization, vitreous/preretinal hemorrhage or preretinal proliferative membrane.	Only microaneurysms (Mild NPDR), or severe proliferative membrane and vitreous hemorrhage covering the retinal characteristics. Any stages with laser spots.
Central Serous Chorioretinopathy (CSCR)	Round or oval macular retinal elevation with distinct margins and turbid fluid underneath, small and yellow sub-retinal deposits. May with depigmented RPE foci or small patches of RPE atrophy or hyperplasia.	Ambiguous retinal elevation with indistinct margins, or liquid partially absorbed leaving macular RPE mottling.

Supplementary Table 17. Diagnosis and numbers of images in non-target categories (NTC) dataset and NTC-JSIEC dataset

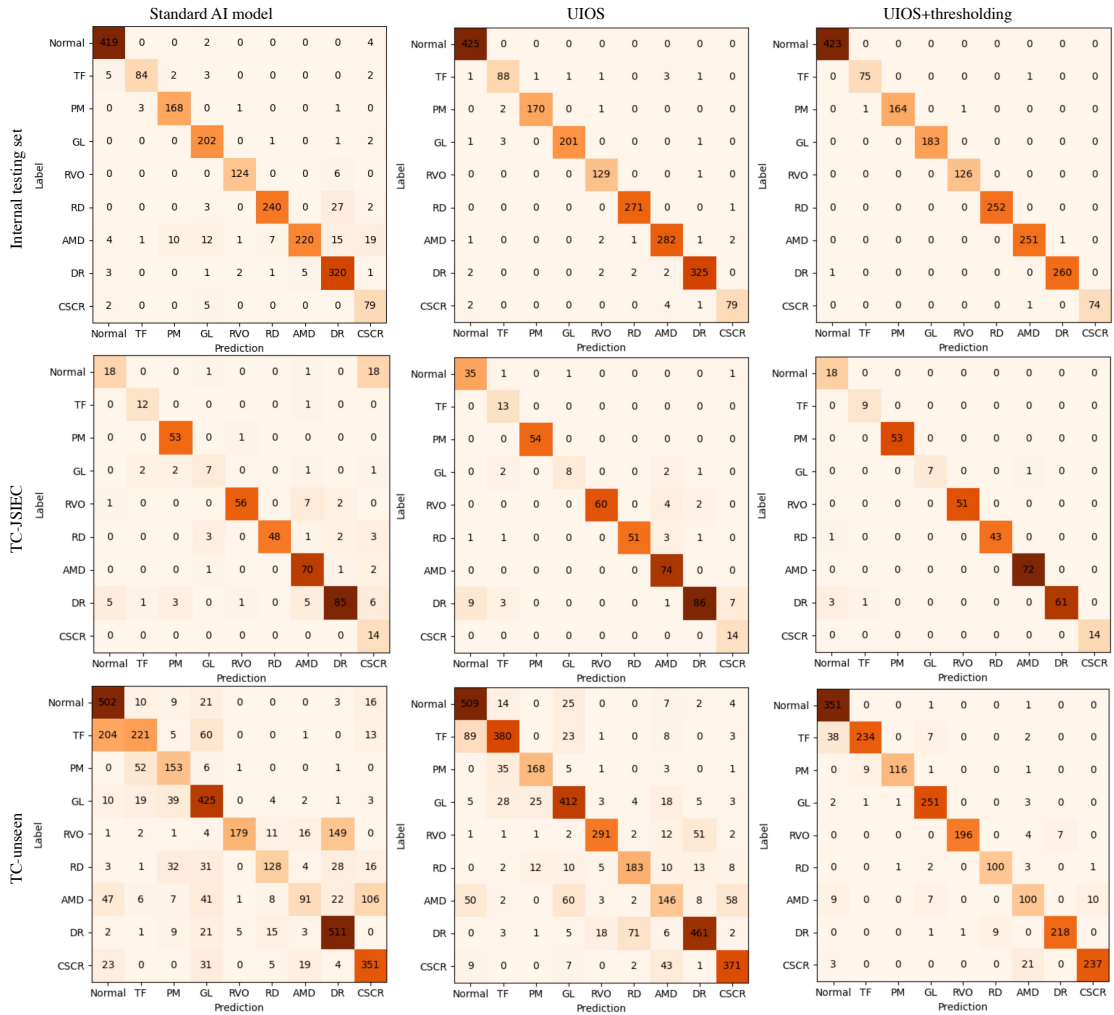
Datasets	number
NTC dataset	1380
Retinal Artery Occlusion	183
Macular Hole	265
Epiretinal Membrane	301
Vogt-Koyanagi-Harada Disease	264
Retinitis Pigmentosa	308
Asteroid Hyalosis	59
NTC-JSIEC dataset	502
Retinal Artery Occlusion	16
Macular Hole	23
Epiretinal membrane	26
Vogt-Koyanagi-Harada Disease	14
Retinitis pigmentosa	22
Asteroid hyalosis	14
Optic atrophy	12
Hypertensive retinopathy	15
Large optic cup	50
Bietti crystalline dystrophy	8
Disc swelling and elevation	13
Dragged disc	10
Congenital disc abnormality	10
Peripheral retinal degeneration and breaks	14
Myelinated nerve fiber	11
Fundus neoplasm	8
Yellow-white spots	29
Vessel tortuosity	14
Chorioretinal atrophy-coloboma	15
Silicon oil in eye	19
Blur fundus	159

Supplementary Table 18: F1 scores (%) of the ablation experiments

Backbone	$L_{UN}$	$L_{TUN}$	Internal testing set	TC-JSIEC	TC-unseen	Average
√	×	×	92.20	80.69	64.74	79.21
√	√	×	94.02	76.05	64.72	78.27
√	×	√	<b>97.29</b>	<b>87.19</b>	<b>77.15</b>	<b>87.21</b>

We conduct ablation experiments to demonstrate the effectiveness of the main components in our proposed UIOS. Supplementary Table 18 shows the ablation results. In our study, the pre-trained ResNet-50 is employed as our backbone for capturing the feature information in fundus images, Backbone+LUN indicates the combination of ResNet-50 and subjective logical (SL) evidential uncertainty theory, while Backbone+LTUN represent our proposed UIOS method. As shown in Supplementary Table 8, compared to the Backbone, Backbone+ LUN to enable the model to generate the prediction with uncertainty score based on the features that were parameterized by Dirichlet concentration. However, as shown in Supplementary Table 18, the F1 score of Backbone+LUN on most testing sets is lower than that of Backbone, mainly because Dirichlet re-parameterization changes the original feature distribution, reducing the model’s confidence in the class-related evidence, thus leading to lower performance. Focusing on this problem, we further improved the loss function by introducing a temperature cross-entropy loss function, which can enhance the model’s confidence in the features that are re-parameterized by Dirichlet, thereby improving the performance in detecting retinal fundus diseases. Thus, it can be seen from Supplementary Table 18 that our proposed UIOS (Backbone+LTUN) achieves the highest performance compared to Backbone and Backbone+LUN on the internal testing set, and two external test sets, the CJSIEC dataset and Non-typical CRD set, both of which have significantly different feature distributions from the training data. The F1 score of our UIOS on three testing set reaches 97.29%, 87.19%, and 77.15%, respectively. These experimental results further demonstrate the effectiveness of our proposed UIOS.



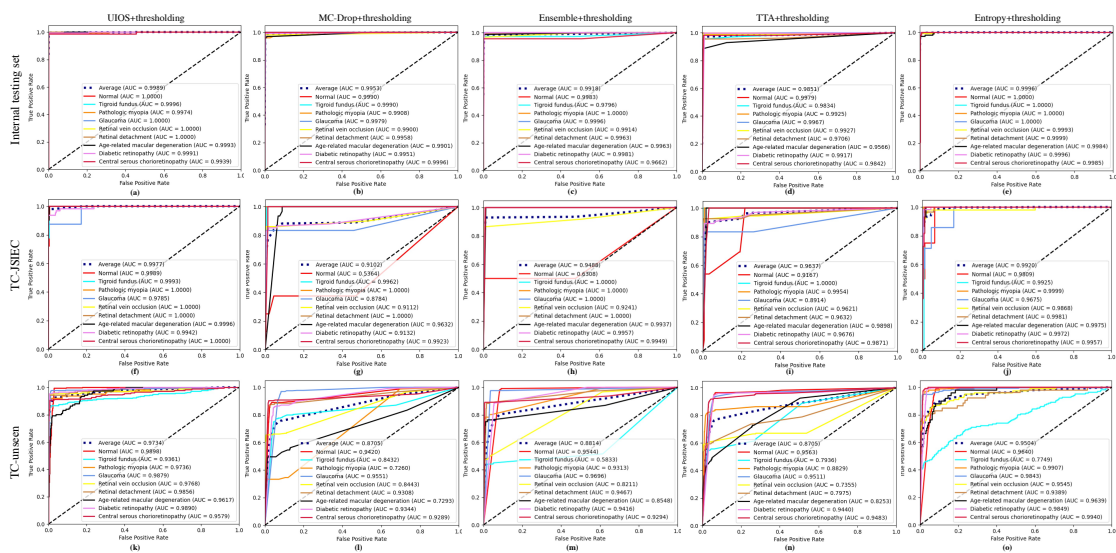


**Supplementary Fig. 1. The confusion matrix of the standard AI model, our UIOS, and UIOS+Thresholding in internal and external testing datasets.**

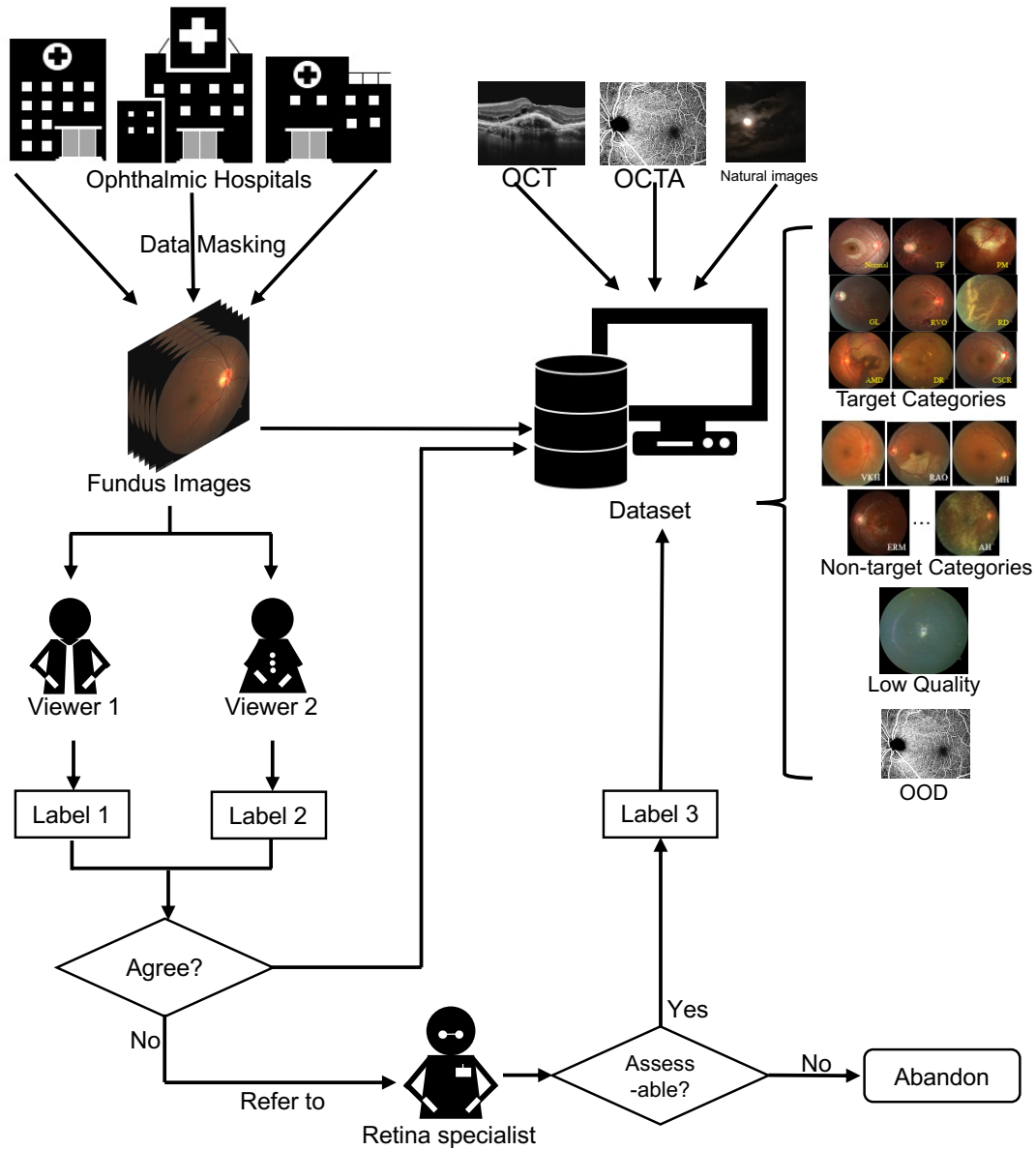
As shown in Supplementary Fig. 1, our UIOS outperformed the standard AI model in terms of confusion matrix for all test sets. Furthermore, when applying our thresholding strategy (UIOS+thresholding) to suggest that samples with uncertainty scores above the threshold seek manual check by an ophthalmologist, we observed a further significant improvement in the confusion matrix and a significant reduction in misclassified samples.



Supplementary Fig. 2. The receiver operating characteristic (ROC) curves of our UIOS model and other uncertainty-based methods in internal and two external testing datasets.



Supplementary Fig.3. The receiver operating characteristic (ROC) curves of our UIOS+thresholding and other uncertainty-based methods+thresholding in internal and two external testing datasets.



Supplementary Fig. 4. Flowchart of the data collection and annotation.